

Article

New Strategy for Creating TiO₂ Thin Films with Embedded Au Nanoparticles

Sofia Rubtsov ¹, Albina Musin ² , Michael Zinigrad ¹, Alexander Kalashnikov ³ and Viktor Danchuk ^{1,*} 

¹ Department of Chemical Engineering, Biotechnology and Materials, Faculty of Engineering, Ariel University, Ariel 4076414, Israel; Sofiar@ariel.ac.il (S.R.); zinigradm@ariel.ac.il (M.Z.)

² Physics Department, Faculty of Natural Sciences, Ariel University, Ariel 4076414, Israel; albinam@ariel.ac.il

³ Rock Capital Partners, 101000 Moscow, Russia; alexander.kalashnikov@gmail.com

* Correspondence: viktorde@ariel.ac.il

Abstract: This paper proposes a new strategy for producing thin films of TiO₂ with embedded gold nanoparticles (TiO₂/AuNP). One of the main tasks was the synthesis of a stable dispersion of TiO₂ and gold nanoparticles in an aqueous solution of ethylene glycol, suitable for inkjet printing—ink with complex gold nanoparticles (AuCNP ink). The AuCNP were synthesized by a reduction from tetrachloroauric acid in the presence of TiO₂ nanoparticles and ethylene glycol (EG). The final formation of TiO₂/AuNP films occurred during the annealing of AuCNP layers, inkjet printed on a glass substrate. The TiO₂/AuNP films demonstrate absorbance in the yellow-green range due to the localized surface plasmon resonance (LSPR) and are promising for solar cell application.

Keywords: gold nanoparticles; inkjet printing; localized surface plasmon resonance; perovskite solar cells



Citation: Rubtsov, S.; Musin, A.; Zinigrad, M.; Kalashnikov, A.; Danchuk, V. New Strategy for Creating TiO₂ Thin Films with Embedded Au Nanoparticles. *Coatings* **2021**, *11*, 1525. <https://doi.org/10.3390/coatings11121525>

Academic Editor: Joaquim Carneiro

Received: 7 November 2021

Accepted: 8 December 2021

Published: 10 December 2021

Publisher's Note: MDPI stays neutral with regard to jurisdictional claims in published maps and institutional affiliations.



Copyright: © 2021 by the authors. Licensee MDPI, Basel, Switzerland. This article is an open access article distributed under the terms and conditions of the Creative Commons Attribution (CC BY) license (<https://creativecommons.org/licenses/by/4.0/>).

1. Introduction

Gold nanoparticles (AuNPs) have a large field of potential applications due to their unique optical and electrical properties, different from their bulk form in many ways. AuNPs have abundant applications in various branches of science, including medicine, materials science, biology, chemistry, and physics [1,2]. Thin-film solar cells with a total thickness of 1–2 μm are of great interest because of the variety of available methods for manufacturing thin layers, the possibility of using different types of materials and substrates, and the economy of materials. The weak point of all thin-film solar cells is that they do not absorb as much light as the massive layer. Therefore, it is necessary to develop methods for capturing light in the submicron layer to enhance the photocurrent and improve the efficiency of the solar cell. One of the methods of light capture is based on the introduction of metallic nanostructures in which LSPR can be excited. The metal nanoparticles (NPs) scatter light, increasing the effective path length within a layer and enhancing light absorption. In addition, hot electrons, induced by plasmons, can facilitate electron transport entering the conduction band of electron transport material [3–5]. Au and Ag metallic nanostructures are the most commonly used because they have good chemical stability and plasmon resonance frequencies in the visible range [6]. It was demonstrated that AuNPs improve device performance in thin-film solar cells of perovskite-type, organic, dye-sensitized ones [6–9]. Therefore, the method of deposition of thin films of metal oxide with embedded AuNPs, proposed in this work, is promising for thin-film solar cells applications.

AuNPs of the desired size, shape and spatial arrangement are required for plasmonic applications. Methods of deposition of AuNPs include spin-coating of NPs synthesized with various chemical routes [3,6,10], sputtering [11,12], and lithographic techniques [13,14]. A promising method for introducing plasmonic structures into the architecture of an electric generating cell is inkjet printing [15]. This method allows one to control the concentration

of NPs in the layer. The introduction of NPs may be performed simultaneously with the deposition of a dielectric matrix, which serves as a functional layer. AuNPs can be prepared by several bottom-up liquid phase routes. One of the most popular methods is the chemical reduction of the precursor salts by sodium citrate (Turkevich's method [16,17]) or other reducing agents, e.g., sodium borohydride [18,19]. After the completion of a chemical reaction, contaminant inorganic salts and ions remain in the product and can be removed only by precipitation and washing of synthesized nanoparticles. The need for multiple purifications of the obtained NPs to ensure a required purity is a drawback for further use in functional layers. Along with the citrate method, the so-called polyol process was developed when polyalcohols were proposed as a class of compounds to produce metal NPs, suitable for various applications such as inks and functional protective coatings. In this process, polyol refers to a diol, such as EG and its derivatives [20]. Basically, a polyol synthesis reduces a metal salt precursor by a polyol species and has certain advantages. Due to the high boiling point of the reducing medium, the synthesis can be carried out at a relatively high temperature. Metal particles are protected from oxidation when they remain in the medium. The high viscosity of the medium and its ability to coordinate metal precursors can minimize coalescence and promote a diffusion-controlled regime for particle growth. All these conditions favor the production of size-controlled crystalline particles. As a rule, the use of the polyol alone is not sufficient to control the size and shape of the particles, so capping agents are added to obtain a desired distribution of NPs. In the early works [21], spherical AuNPs were synthesized in EG in the presence of polyvinylpyrrolidone (PVP), which prevented aggregation of NPs. It was shown that the size of the AuNPs might be controlled by varying the concentration of nonionic surfactant Tween 80 (polyethylene glycol sorbitan monooleate) during the reduction of tetrachloroauric acid by maltose [1]. Molecules of Tween 80 interacted with growing gold nuclei, formed during the initial phase of the reduction process, and blocked their surface. The formation of new nuclei was preferred over the further growth of the preformed ones.

An important class of materials, usually used as supported metal catalysts, includes the NPs deposited/embedded onto a solid support. The support material is essential in determining the catalytic behavior of supported AuNPs; both organic polymers and inorganic materials got quite a lot of attention in the literature [22,23]. In a typical liquid-phase synthesis procedure for metal oxide supported AuNPs, preformed metal oxide particles are mixed with an aqueous solution of HAuCl_4 , and the necessary additives, stirring is performed, followed by washing a suspension, drying, and calcining. Similar methods have been used to deposit Au on oxide supports such as TiO_2 , Fe_2O_3 , Al_2O_3 , MgO , and others [22,24,25]. Reduction of Au(III) to Au(0) presumably occurs in several stages. It begins with the adsorption of gold chloride and gold chloro-hydroxy $[\text{Au}(\text{OH})_{4-x}\text{Cl}_x]^-$ complexes on a surface of metal oxide particles via electrostatic interaction or ligand exchange. It was suggested [25,26] that the gold chloro-hydroxy species interact with surface M–OH groups present at the oxide–water interface by the mechanism:



where M is a metal, and the OH group is the result of the dissociative water chemisorption. With some kind of reducing agent or by irradiation, the Au complex can be subsequently reduced to Au clusters, agglomerating to AuNPs on the surface of the support oxide particles. It was demonstrated [26] that HAuCl_4 reduced spontaneously in EG in the presence of preformed ZnO nanoparticles at room temperature, without any additional stabilizers, forming Au/ZnO nanostructures with a pronounced plasmonic band in the absorption spectra. Considering the reaction (1), the authors [26] assumed that the electrostatic attraction between gold chloride (or chloro-hydroxyl complexes) and a positively charged ZnO surface promoted close contact and chemical adsorption of gold precursors by replacing one of the chloride ligands with a hydroxyl group on the ZnO surface. The reaction between Au and EG led to the reduction of Au(III) to Au(I) and eventually to Au(0). The further agglomeration of Au(0) species resulted in the formation of Au NPs, which was

confirmed by the appearance of a plasmon band in the absorption spectrum of the solution of precursors. It was noticed that the plasmon band appeared only after the decay of the absorbance of Au(III) species [26]. In the liquid-phase reduction method, the combination of components and the order of their introduction into the reactor affects the size of Au NPs and, accordingly, the catalytic activity of the obtained materials [27]. Typically, small Au NPs (2–5 nm) have higher activity, and the catalytic performance is sensitive to the preparation method and residual chloride content. The metal oxides supported reduction is a recognized method for preparing catalysts, so the catalytic properties of Au/metal oxide complex NPs are the most studied [28,29].

However, similar techniques can be used to synthesize NPs for other applications, particularly for introducing them into thin layers by printing or spin coating to create functional layers with LSPR properties. In this work, we aimed to develop a method for synthesizing ink, that is, a stable dispersion of AuCNP in a liquid medium, to print thin films based on TiO₂ with embedded AuNPs. This ink may be further used for inkjet printing without any additional operations. After deposition and annealing, thin TiO₂ layers, including AuNPs surrounded with TiO₂ (TiO₂ with embedded gold nanoparticles, TiO₂/AuNP), may be manufactured. The interest in a method for synthesizing print-ready inks is twofold. First, it can provide a direct synthesis of Au NPs with a functionalized surface. Second, the kinetics of AuNPs growth should be determined by both the synthesis and deposition conditions, that is, a degree of surface coverage during the deposition of a layer and further heat treatment processes. We assume that this method of manufacturing functional layers can find a wide range of applications, for example, in thin-film solar cells, sensors, and molecular electronics.

2. Experimental Section

The TiO₂ NPs (TNP) were synthesized with a sol-gel method, described in the Supplementary Materials (SM), using titanium isopropoxide (Ti[OCH(CH₃)₂]₄, 99.995%, Alfa Aesar, Lancashire, UK), nitric acid (HNO₃ 70%, Daejung, Siheung-si, Korea) and isopropanol (C₃H₈O Carlo Erba, Cornaredo, Italy). Ink with gold complex nanoparticles (AuCNP) was synthesized from hydrogen tetrachloroaurate(III) trihydrate (HAuCl₄·3H₂O 99.99%, Alfa Aesar), ethylene glycol (Daejung), and surfactant Tween 80 (Sigma-Aldrich, Hamburg, Germany). Bidistilled water (DI) (Milli-Q[®] IQ 7003, Merck, Darmstadt, Germany) was used in all experimental procedures.

2.1. Preparation of AuCNP Ink

The ink presenting a dispersion of AuCNP and TNP in the mixture of EG and water was prepared with a modified polyol method on TiO₂ support [25]. The 0.125 g of TiO₂ NPs xerogel (see Supplementary Materials) was dissolved in 6 mL EG and 2 mL DI water. The prepared colloid solution was heated till 150 °C in a flask immersed in an EG bath; vapors were cooled in a jacketed double coil condenser (44 cm length) with circulating water at 15 °C and returned to the flask. The acid solution consisted of 0.0677 g HAuCl₄·3H₂O mixed with 2 mL DI water and 1.2 µL Tween 80, which was quickly injected into the flask with boiling TiO₂ colloid. The mixture was boiled for 10 min under constant intensive stirring (500 rpm) with a magnetic stirrer. Next, the resulting dispersion of AuCNP was cooled to room temperature and stored at 8 °C in a lab refrigerator.

2.2. Printing Methods

Continuous AuCNP ink layers were deposited on 25 mm × 25 mm Soda Lime (Corning, Corning, NY, USA) glass substrates with Dimatix Materials printer DMP 2850 (Santa Clara, CA, USA) with a 10 pL cartridge. The substrates were preliminary cleaned according to the protocol, presented in Supplementary Materials, and treated for 2 min in RF plasma (Plasma Cleaner, MTI Corporation, Richmond, CA, USA) in residual oxygen at air pressure in the chamber at 200 mTorr, “High” mode for 2 min. Before filling a cartridge, the AuCNP ink was filtered with a 0.22 µm filter (Jet Biofil, Guangzhou, China). The printing process

was carried out with a jetting frequency of 5 kHz, and the voltage on the nozzles was varied in the range of 19 to 25 V. The ink was printed on glass substrates with a drop spacing of 40 μm in three layers. As the contact diameter of a single drop on glass was about 80 μm , that is, larger than the drop spacing, jetted drops merged and formed a continuous layer. After deposition, the samples presenting a continuous thin layer of ink on glass substrate were sintered at 550 $^{\circ}\text{C}$ for 30 min with a continuous 10 sccm oxygen flow (ALIMC-500 ccm, Alicat Scientific, Richmond, CA, USA) in the tube furnace KJ-T1200 (Zhengzhou Kejia Furnace Co., Ltd., Zhengzhou, China). Estimates carried out on the assumption that all components of the ink had completely reacted and all AuNPs were embedded in the TiO_2 matrix after printing and annealing, give 23 wt% of the Au content in the TiO_2 matrix after film annealing.

2.3. Characterization Methods

Particle size and zeta potential values were measured using LightsizerTM 500 instrument (Anton Paar GmbH, Graz, Austria). All dispersions were diluted 1:30 with DI water. Particle size measurements were performed by the dynamic light scattering (DLS) method at 10 $^{\circ}\text{C}$, the refractive index of a solvent was set as for water [30]. The stability of NPs in dispersion was evaluated by the zeta potential using electrophoretic light scattering (ELS) [31]. The ELS measurements were made at 25 $^{\circ}\text{C}$ with a maximum voltage of 200 V. The rheological and physical properties were evaluated to determine the ink printability. The viscosity of the AuCNP ink was evaluated with a DVE viscometer (Ametek Brookfield, Middleborough, MA, USA) at 100 rpm of spindle S18. A Sigma Attension 703D tensiometer (Biolin Scientific, Gothenburg, Sweden) was used for the surface tension measurements by Du Nouy's method. The density of the AuCNP dispersion was calculated from mass and volume measurements with a pycnometer 10 mL. All measurements were completed at the same conditions at 25 $^{\circ}\text{C}$.

Measurements of acidity/basicity of ink solutions with and without adding HAuCl_4 —pH and oxidation rate reaction (ORP)—were carried out with a Multi parameter Analyzer DZB-712 (INESA Scientific Instrument, Shanghai, China) at room temperature.

The contact angle was measured with optical microscope MXB 5000REZ (Hirox Co., Tokyo, Japan), for a 5 μL droplet placed on a glass substrate, cleaned the same way as for printing. Measurements were made for three solutions: EG:H₂O 3:2 (liquid base of the ink), TiO_2 colloidal NPs in the liquid base, and AuCNP ink.

Thermal decomposition and compounds scans experiments were performed with a thermogravimetric analysis (TGA) (Pyris 1, PerkinElmer, Waltham, MA, USA). TGA measurements were carried out in the temperature range from 35 to 600 $^{\circ}\text{C}$, at a heating rate of 10 $^{\circ}\text{C}/\text{min}$, and a gas flow (N_2) of 20 mL/min.

The morphology of AuCNP ink films was studied with a TESCAN MAIA3 (Brno, Czech Republic) scanning electron microscope in SEM and scanning transmission electron microscopy (STEM) mode. The crystalline structure of the films was determined with an XRD Rigaku SmartLab SE (Rigaku, Tokyo, Japan) diffractometer with a $\text{CuK}\alpha$ source. The size distribution of AuNP embedded in the TiO_2 matrix was evaluated by analysis of SEM images with ImageJ (version V 1.53, 2021, University of Wisconsin, Madison, WI, USA) software using a modified "Particle size" plugin. The absorbance of the films was measured with a spectrophotometer UV-Vis GENESYS 10 (Thermo Scientific, Waltham, MA, USA) in the wavelength interval from 400 to 800 nm. The Raman spectra were recorded with Enspectr R532 (Enhanced Spectrometry Inc., Meridian, ID, USA) in a scanning range of 160–1600 cm^{-1} .

3. Results and Discussion

3.1. Characterization of the AuCNP Ink

The synthesized dispersion of AuCNP, including inorganic and organic species, was stable and repeatable. To study the composition of the dispersion, five types of solutions were prepared, described below, and their parameters were measured and compared:

- N1—The solution of EG/H₂O 3:2 by volume, that is the ink's base liquid components.
- N2—The colloid solution of TNP in EG/H₂O 3:2 without adding HAuCl₄.
- N3—The AuCNP precursor, which is the mixture of all ink components without heating and boiling, with stirring only.
- N4—The water AuCNP ink without EG.
- N5—The AuCNP ink.

The detailed description of the samples N1–N5 is presented in Supplementary Materials (see Figure S1).

The mean hydrodynamic diameter (HDD) of particles, measured with “Lightsizer™ 500”, for N3, N4, and N5 dispersions, is presented in Figure 1A. Immediately after the synthesis, the HDD of AuCNP ink (N5) was about 270 nm with a relatively wide size distribution. Unlike the N5 ink, the scattering plots from the N4 and N3 dispersions include two maxima, indicating the presence of two groups of particles of different sizes in the solutions. The first group with an average diameter of 40 nm corresponds to TNP (see Figure S2), and the other (370 nm) to AuCNP. Therefore, adding EG and heating and boiling the ink precursor is necessary for forming the homogeneous AuCNP dispersion.

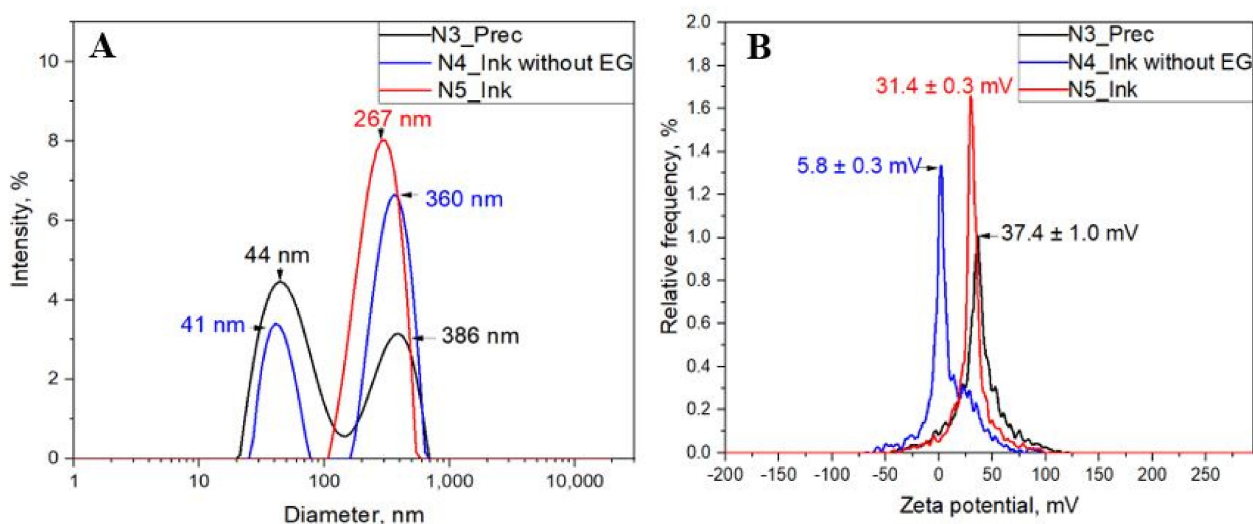


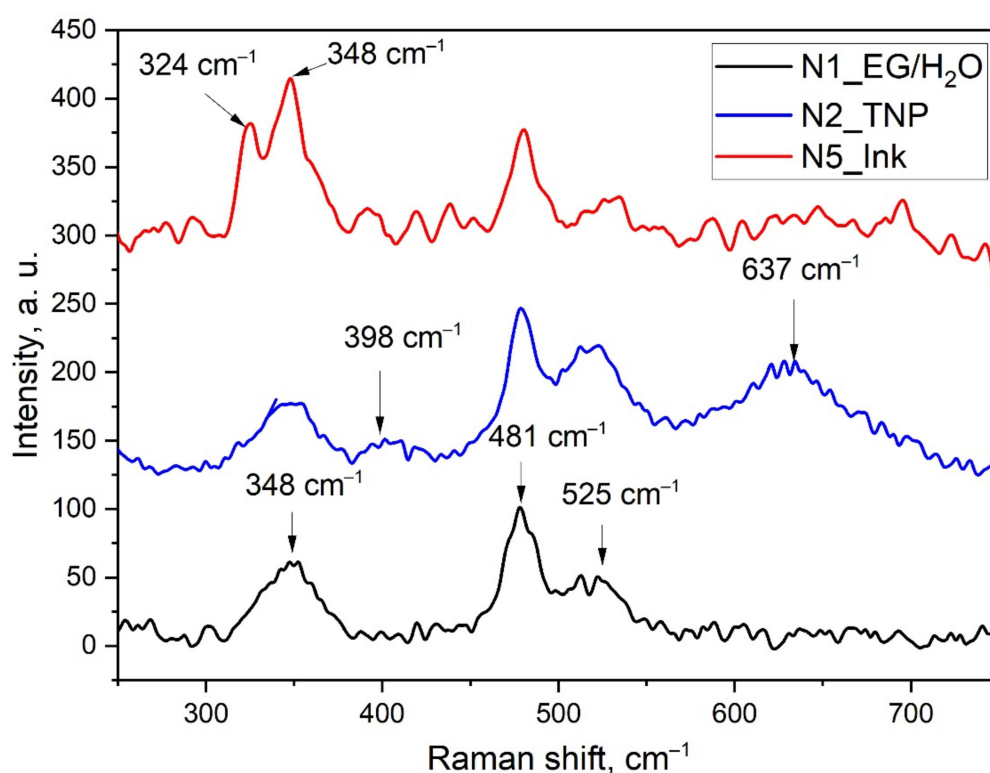
Figure 1. (A)—Particle size distribution and (B)—zeta potential of colloidal AuCNP obtained by DLS and ELS, respectively, ink precursor—black curves, AuCNP ink—red curves, and AuCNP ink without EG—blue curves.

The values of zeta potential and pH of the N2–N5 dispersions are presented in Figure 1B and Table 1, correspondingly. Let us pay attention to the fact that the pH for all these dispersions is acidic (see Table 1) since they are based on the N2 dispersion. The zeta potentials of the samples N2, N3, and N5 differ insignificantly and are close to 30 mV, which, according to [31], corresponds to dispersions with optimal stability, whereas the zeta potential of the N4 dispersion is much less and equals 5.8 mV, which is one of the reasons for its instability. Indeed, visible precipitation of the N4 dispersion occurred within an hour after preparation, while the N2 and N5 dispersions remained stable even after several months. This fact indicates the decisive role of EG in the formation of stable AuCNP ink. We supposed that the particles with a size range from 250 to 400 nm are an agglomerate of TiO₂ NPs, nascent Au clusters, ionic species of HAuCl₄ decomposition, and EG molecules (AuCNP) [25–27,32–35].

Table 1. pH and zeta potential values.

Sample	Composition	pH, $\pm 0.01\%$	Zeta Potential, mV
N2	TiO ₂ colloid	0.45	30.0 \pm 0.3
N3	Ink precursor	1.04	37.4 \pm 1.0
N4	AuCNP without EG	1.94	5.8 \pm 0.3
N5	AuCNP ink	0.62	31.4 \pm 0.3

The Raman spectra of the N1, N2, and N5 dispersions are presented in Figure 2. Recall here that the N5 is the final AuCNP ink, the N2 is the TNP (colloid solution of TiO₂ NPs in EG/H₂O 3:2), and the N1 is the solution of EG/H₂O 3:2 by volume, which is the liquid base for both N5 and N2. The Raman lines at 348, 481, and 525 cm⁻¹ present in the spectra for all dispersions were assigned to a C–C–O torsional and bending modes in EG [36].

**Figure 2.** The Raman spectra of the N1, N2, and N5 dispersions.

Comparative analysis of the presented Raman spectra revealed two characteristic features. The first is the presence of bands at 324 and 348 cm⁻¹ in the spectrum of N5, which correspond to the stretching of Au–Cl in [AuCl₄]⁻, indicating the presence of these species in the AuCNP ink even after heating and boiling [32]. It should be emphasized here that the 348 cm⁻¹ peak is also present in the Raman scattering spectrum of EG. However, for the N5 dispersion, this peak is more intense than for N1 and N2 since it is a superposition of the corresponding EG and Au–Cl peaks. Thus, this suggests that during the synthesis of the ink, some of the gold remains unreduced. In the N5 spectrum, the absence of peaks in the range of 560–580 cm⁻¹, related to the stretching vibrations of Au–OH, is consistent with the chloro-hydroxyl compounds of gold identified in solutions containing gold(III) chloride at low pH [32,33]. Note that the isoelectric point (IEP) of the support is of great importance in the metal-oxide-assisted reduction of Au NPs. When the pH of the solution is higher than its IEP, the adsorption of cations on the surface of the support particles occurs; otherwise, anions are adsorbed [34]. The IEP of TiO₂ is 6.0, and the pH values of both N5 and N2

dispersions are less than 1 (see Table 1); therefore, it is quite possible that the formation of a surface gold complex is initiated by the $[\text{AuCl}_4]^-$ anion adsorption on the TiO_2 surface. The other feature is the presence of peaks at 398 and 637 cm^{-1} in the N2 spectrum, which are characteristic of the TiO_2 anatase phase [35], and a significant reduction in the intensity of these peaks in the N5 dispersion. This fact is one more evidence of TNP participation in the formation of AuCNP agglomerates.

For ink, in addition to the characteristics of suspension, surface tension and viscosity are important parameters. Surface tension, viscosity, and density of the dispersion are the basic properties defining the formation and behavior of liquid jets and drops. The combination of these parameters, expressed by the dimensionless Ohnesorge number, is usually used for evaluating the printability of ink:

$$\text{Oh} = \frac{1}{Z} = \frac{\eta}{\sqrt{\gamma\rho d}} \quad (2)$$

where η is the fluid's viscosity, γ —surface tension, ρ —density, and d —the characteristic dimension (diameter of the jet nozzle or drop). The rheological properties of the ink are presented in Table 2. The Z parameter for the reciprocal Ohnesorge number defines the range over which liquids can be printed as $10 > Z > 1$ [37–39]. d is the size of the silicon nozzle and is approximately 21.5 μm . It can be concluded (see Table 2) that the rheological properties of the AuCNP ink are in a stable range for printing.

Table 2. Rheology parameters of the synthesized AuCNP ink.

Sample	Composition	Viscosity, cP, ± 0.2	Surface Tension, N/m, ± 0.5	Density, g/cm^3 , ± 0.05	Z , ± 0.1	Contact Angles, $^\circ$, ± 0.5
N1	EG/ H_2O 3:2	4.9	54.2	1.10	7.30	13.9
N2	TNP	5.2	53.4	1.11	6.87	16.7
N5	AuCNP ink	9.7	52.8	1.11	3.60	18.3

Besides the rheological properties, the wettability is also critical for the formation of a uniform layer. The contact angle measurements presented in Table 2 show that the contact angles of the TNP and AuCNP inks are only slightly larger than for the EG/ H_2O solution, and in all cases, are less than 20° . Consequently, TNP and AuCNP dispersions perfectly spread over the surface of the glass substrate, which contributes to the formation of uniform continuous layers.

In addition to the dispersion characteristics and the methods and modes of deposition of layers, the determining factor for forming homogeneous uniform films is the procedure of their temperature treatment (drying and annealing). In order to correctly set the parameters of the temperature treatment of the layers and reveal the process of the film formation, a TG analysis of dispersions N1, N3, and N5 was carried out. The TG and DTG data are presented in Figure 3A,B, respectively.

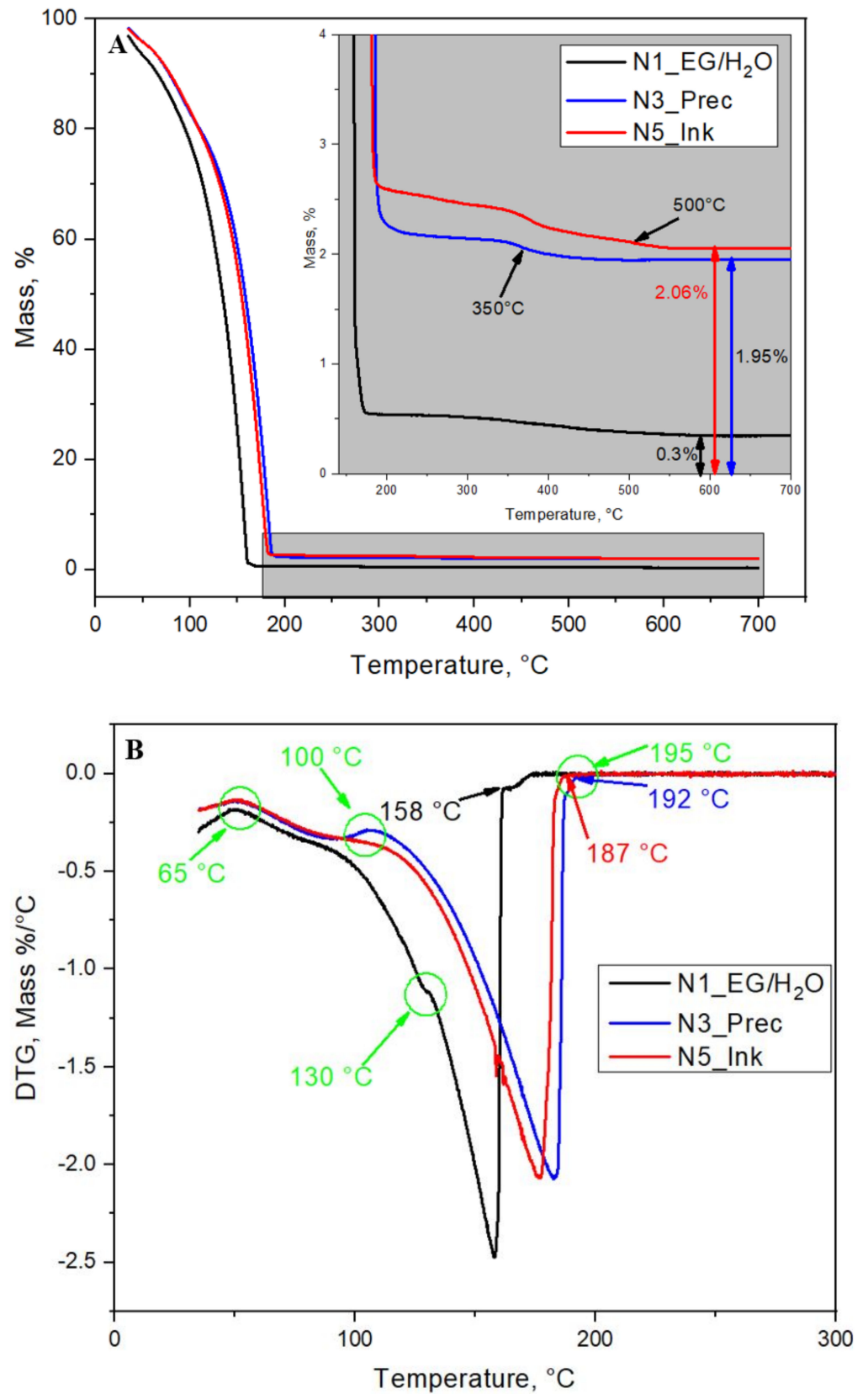


Figure 3. (A) The data of TG analysis: the gray insertion demonstrates the peculiarities of the high-temperature tails. (B) The data of DTG analysis: the green arrows point to the hidden features in TG data.

The thermogravimetric (TG) and differential thermogravimetric (DTG) analyses show thermal mass loss and its rate during thermal decomposition. For all samples, the interval of 30–200 °C corresponds to the continuous mass loss due to the evaporation of water, EG, and other volatile components. The mass lost for the N1 sample was 99.7% which means that all the EG/H₂O solution was evaporated during the heat treatment. For dispersions N3 and N5, the mass loss during the TG analysis was 98.05% and 97.94%, respectively. Consequently, about 2% of solid sediments remained after the heat treatment of each of the dispersions (see gray insertion in Figure 3A). These values are positively correlated with the theoretical estimate (1.76 wt%) of the NPs mass contained in the AuNCP ink. The displacement of the evaporation point for dispersions N3 and N5 to higher temperatures than N1 and the presence of inflections in the temperature range of 300 and 500 °C is due to the presence of solid nanoscale formations, from which the removal of volatile components requires more energy. The DTG analysis revealed several temperature regions at temperatures about 65, 100, 130, and 195 °C, which are highlighted with green circles in Figure 3B, and are associated with the predominance and overlap of the evaporation processes of various volatile components, the reduction of AuNP, and the formation of AuCNP in the N3 and N5 dispersions. These temperatures were considered for developing the film annealing regime presented in Figure 4.

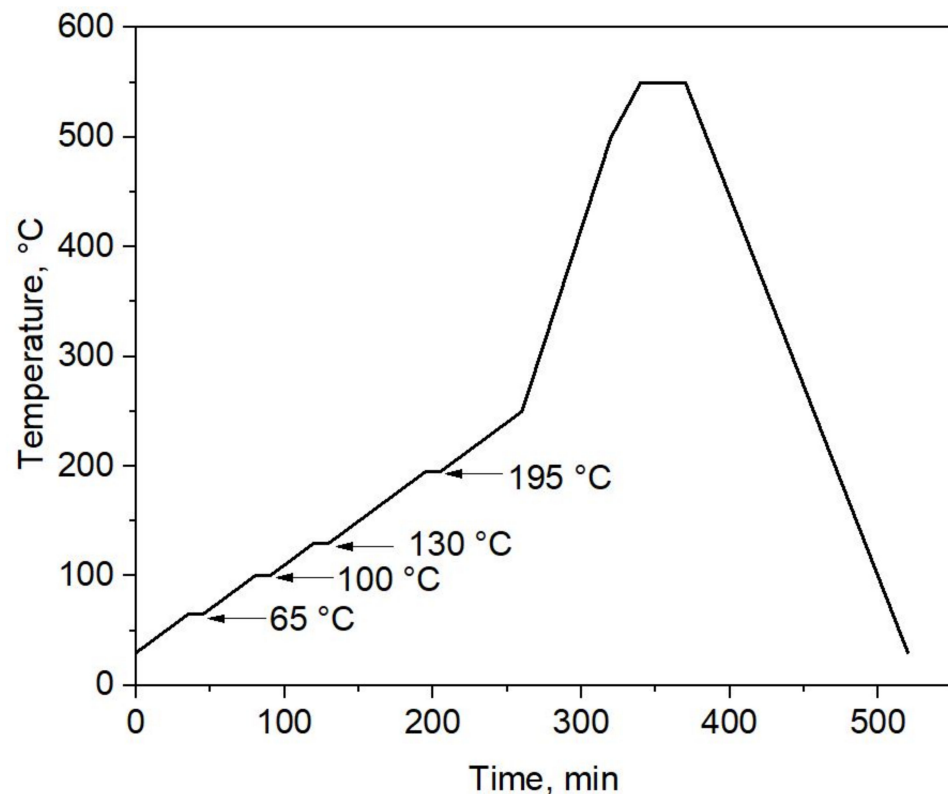


Figure 4. The annealing thermogram for the AuCNP ink.

Based on the ongoing processes, the presented thermogram can be divided into four ranges. In the temperature range from 30 to 100 °C, including 10 min stabilization shelves at 65 and 100 °C, the process of water evaporation prevails. In the second temperature range (from 100 to 195 °C) with stabilization shelves at 130 and 195 °C, the evaporation of EG/H₂O solution and other volatile composites occurs, and the TiO₂-supported Au reduction processes continues. In the third temperature range (from 195 to 550 °C with a 30 min shelf at 550 °C), the final removal of volatile residues and the formation and annealing of the TiO₂ matrix with embedded AuNPs is completed. Note that the entire temperature treatment process of the films was carried out with continuous blowing of the furnace chamber with dry air at a flow rate of 10 sccm. The heating rate was 1 °C/min

from 30 to 250 °C, then it was increased fivefold for the range of 250 to 500 °C and finally maintained at 2 °C/min at temperatures from 500 to 550 °C. The cooling rate was 5 °C/min.

In order to elucidate the morphology and size of the particles in the ink, as well as the particles forming on a substrate during drying and annealing, the AuCNP ink was dripped on Cu grids and treated at different temperatures. The STEM images of drops of ink on copper grids after different treatments, i.e., dried at room temperature, heated to 200 °C, and annealed at 550 °C, are presented in Figure 5. We emphasize that the temperature treatment of the samples was carried out in the same furnace, under the same blowdown modes, and according to the corresponding stages shown in the thermogram (Figure 4).

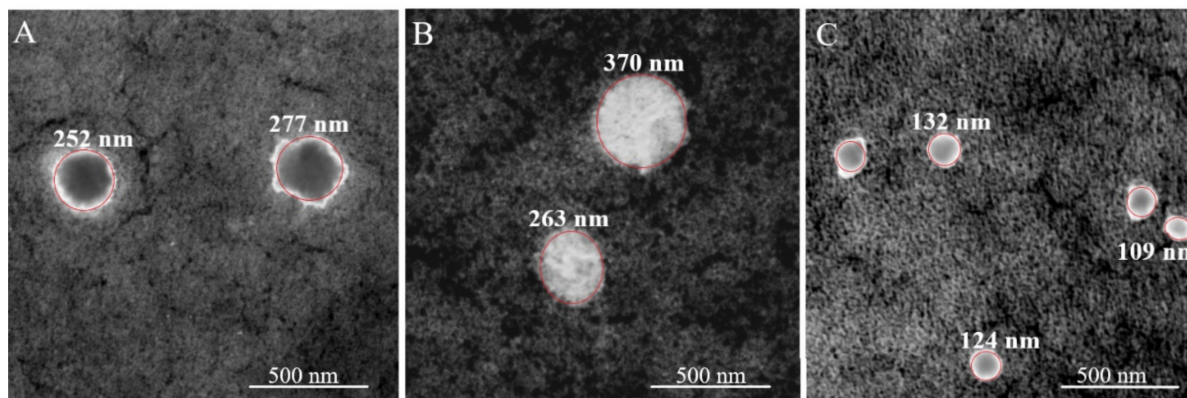


Figure 5. STEM images of the AuCNP evolution in the process of different thermal treatments: (A)—drying at room temperature, (B)—200 °C heating, (C)—annealing at 550 °C.

The diameter of AuCNPs dried at room temperature (Figure 5A), is in the range obtained from the DLS measurements. Their shape was not spherical but more like a drop spreading over a surface. Moreover, it can be seen that the adsorption contrast of the inner parts of AuCNP particles is not uniform, so they actually look like merged, smaller NPs. After heating at 200 °C and evaporation of EG/H₂O (Figure 5B), there was no significant change in the diameter of the AuCNPs. In this case, we registered bright scattered signals over all the surfaces of the particles, which look like an inhomogeneous 2D agglomerate of smaller AuNPs. During the annealing at 550 °C (Figure 5C), the agglomerated NPs merged and formed globular AuCNPs with an average diameter of about 100 nm. In all three images, the AuNPs are embedded in a TiO₂ film, the lower absorption contrast of which, in comparison with the AuNPs, causes its darker display on STEM images. During the subsequent heat treatment, volatile components are removed, and the film becomes more compact and thinner, and, as a result, its signal (Figure 5C) becomes more intense.

3.2. Characterization of TiO₂/AuNP Films

Three layers of AuCNP ink sequentially, one on top of the other, were inkjet printed onto a glass substrate. After the printing of each layer, it was dried for two minutes at room temperature. Then, this composite layer was temperature treated according to the thermogram (Figure 4) to form a TiO₂/AuNP film with a thickness of 120 nm (see Figure S3). The thickness of the films was estimated from the cross-sectional SEM data (see Figure S4).

The XRD analysis of the TiO₂/AuNP films is presented in Figure 6. The synthesized coatings were continuous homogeneous transparent polycrystalline films.

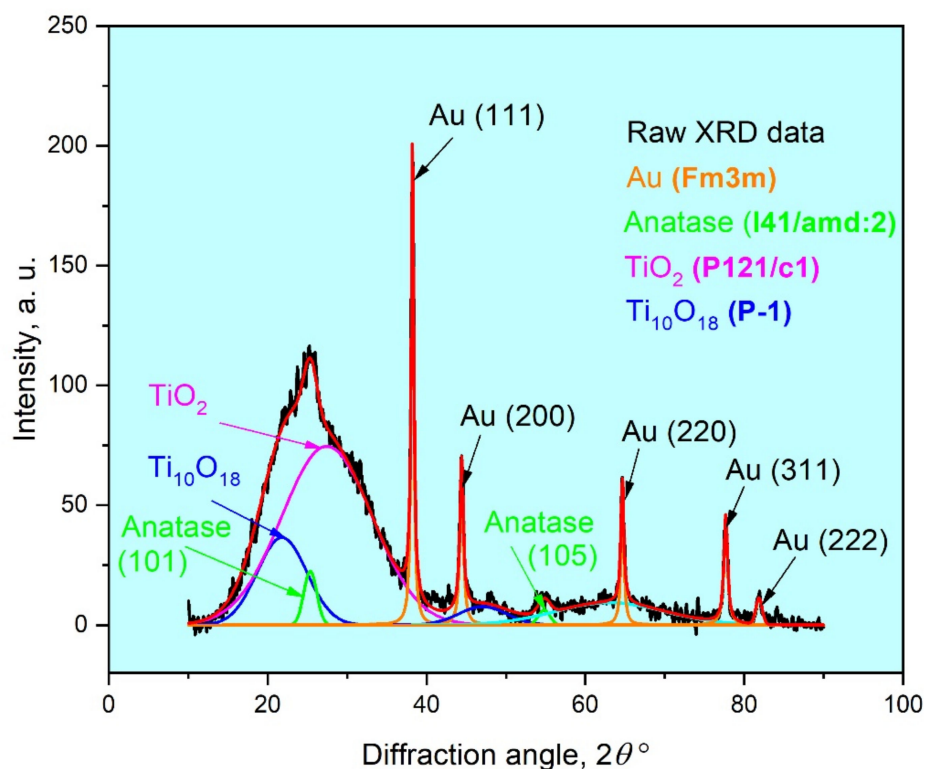


Figure 6. XRD pattern from TiO_2/AuNP film inkjet printed with 7-day-aged ink on a glass substrate and annealed at 550°C . The black line is the raw X-ray data. The red line is the fitted data as a result of the peak deconvolution analysis. The blue, green, pink, and orange lines present the peaks that belong to $\text{Ti}_{10}\text{O}_{18}$, Anatase, TiO_2 , and Au (Fm3m) phases, respectively.

A pronounced halo in the low-angle region and a peak at the position $2\theta = 25^\circ 37'1''$ correspond to a superposition of diffraction reflections from three phases of titanium oxide: $\text{Ti}_{10}\text{O}_{18}$, TiO_2 , and anatase constituting 21, 75, and 4% of the matrix, respectively. The $\text{Ti}_{10}\text{O}_{18}$ and TiO_2 phases are ultradisperse with a coherent scattering region (CSR) of 6 \AA and 12 \AA , respectively, the CSR of the anatase phase is 50 \AA . Sharp, well-defined peaks in the diffractogram correspond, in angular positions, to the fcc gold phase. The CSR of this phase is 127 \AA . Thus, according to the X-ray diffraction analysis data, the TiO_2/AuNP film consists of three TiO_2 phases, two of which are ultradisperse, and the fcc phase of AuNP. The aging stability of the ink and, as a consequence, the reproducibility of the printed films is the cornerstone of their applicability. The XRD analysis did not reveal a significant difference in the films printed with 1-, 2-, and 7-day-aged inks. The corresponding diffractograms are presented in Figure 7.

A full-profile analysis of the 7 day diffractogram is shown above in Figure 6. Note that the positions, shapes, and intensities of both the TiO_2 halo and the gold peaks did not change with the aging of the ink. More informative in this regard were the results of SEM studies of the morphology of TiO_2/AuNP films. The SEM images of the surface of TiO_2/AuNP films printed with 1-, 2-, 7-, 10-, and 19-day-aged inks and labeled D1, D2, D7, D10, and D19, respectively, are shown in Figure 8. It has been found that the age of the AuCNP ink, meaning how many days have passed since the ink was prepared, is a critical parameter affecting the AuNP size distribution in the TiO_2/AuNP films.

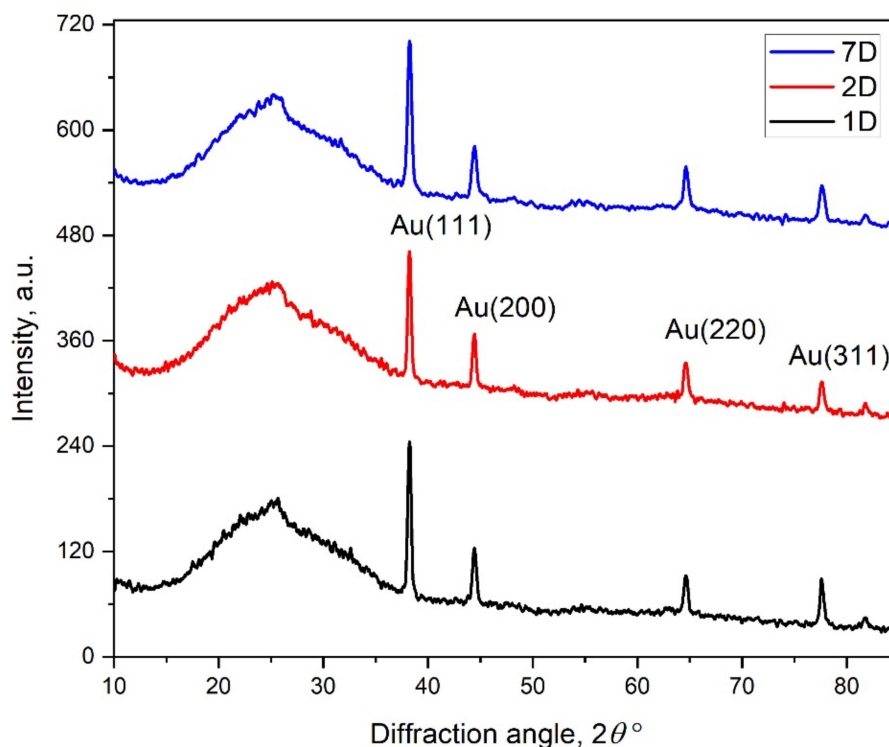


Figure 7. The XRD data of TiO_2/AuNP films printed with 1-, 2-, and 7-day-aged AuCNP inks.

The agglomerates of AuNPs with mean sizes of 80 and 40 nm and a standard deviation (SD) of 30 nm were detected in the D1 and D2 films, respectively. Aging of the ink within seven days of preparation or more led to a significant decrease in the SD and an improvement of the AuNPs size distribution in the TiO_2/AuNP films. The AuNP particles with mean sizes of 63, 29, and 33 nm with a SD of 15 nm were revealed in the films D7, D10, and D19, respectively. We emphasize that, within the measurement error, the mean sizes of AuNPs particles in TiO_2/AuNP films printed with 10 and 19 day ink did not change and, on average, were equal to 30 nm. The size distribution and SD of the AuNP in the TiO_2/AuNP films for the inks at the different storage time, restored from the corresponding SEM images, are presented in Figure 8. Importantly, note that regular monitoring of ink during storage and immediately before printing did not reveal sedimentation processes in them. The HDD of AuCNP particles in dispersion did not change, and the ink remained stable even four months after synthesis (see Supplementary Materials, Figure S5).

The absorption spectra of the TiO_2 and TiO_2/AuNP films printed with TNP dispersion and 10-day-aged inks, respectively, and spherical-shaped AuNPs in water (W/AuNP) [40] are shown in Figure 9. The absorption at 571 nm in TiO_2/AuNP film and 543 nm in W/AuNP are explained by localized surface plasmon resonance (LSPR) of AuNPs.

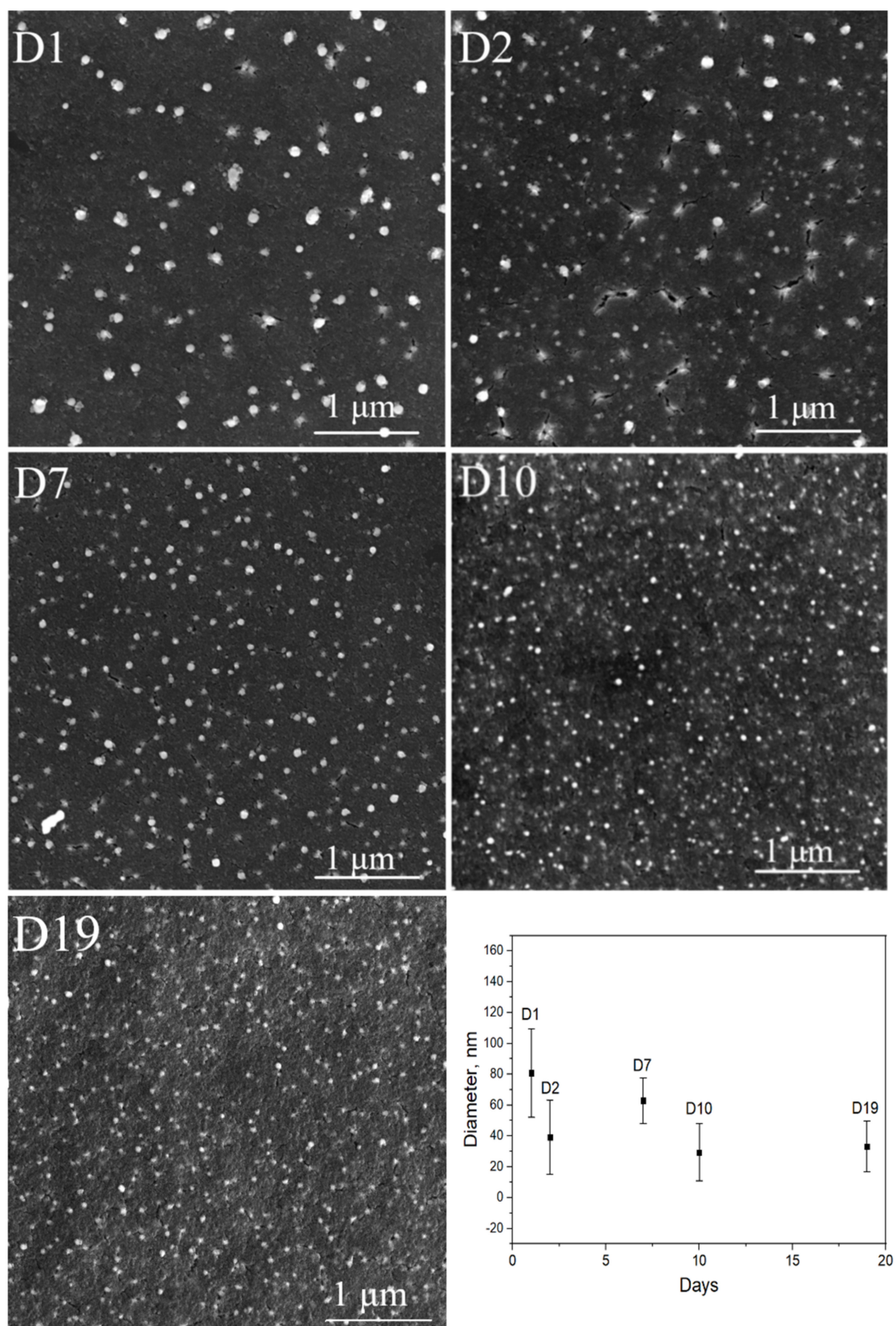


Figure 8. SEM images of the TiO₂/AuNP films printed with the inks of different day-age and the day-age dependence of the size distribution of AuNPs in these films. The bars in the plot correspond to the standard deviation of the size. D1, D2, D7, D10 and D19 on subfigures correspond to 1-, 2-, 7-, 10-, and 19-day-aged inks.

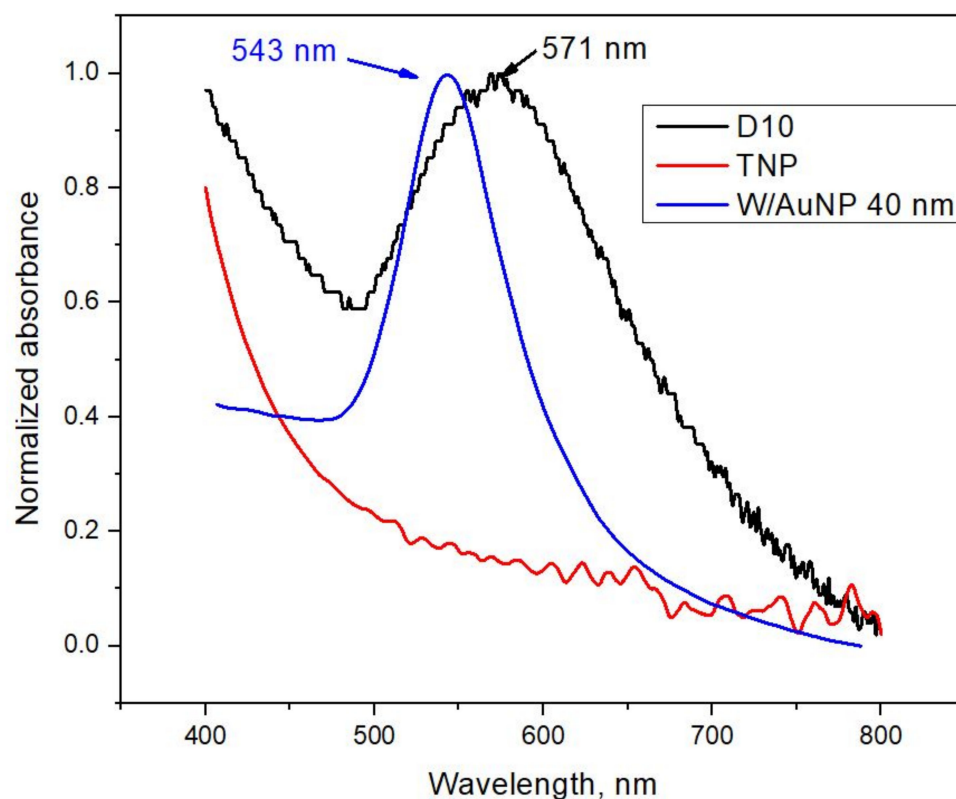


Figure 9. Normalized absorbance spectra of TiO_2 , D10 TiO_2/AuNP ink-jet printed films, and 40 nm AuNPs dispersed in water [40].

The peak position of plasmonic absorption is sensitive to the size of AuNPs and the surrounding dielectric environment [41,42]. The average diameter of the AuNPs in the D10 TiO_2/AuNP film is 29 nm (see the plot in Figure 8); however, the corresponding plasmon absorption peak is shifted to the red region, relative to the one of the W/AuNP dispersion, the average particle size of which is 40 nm. This shift is caused by the fact that AuNPs in D10 TiO_2/AuNP films are surrounded by the TiO_2 matrix, whose dielectric constant [43] is higher than that of water. The AuNPs are embedded in the TiO_2 matrix and cause the LSPR absorption of light by the TiO_2/AuNP films in the yellow-green wavelength range. Moreover, by varying the AuNP size, shape, and dielectric environment, this range can be tuned to improve SC absorption.

4. Conclusions

A new strategy for depositing thin TiO_2 films with embedded AuNPs for SC applications was proposed. The films were inkjet printed with AuCNP ink on glass substrates. The method of polyol synthesis of gold nanoparticles on a metal oxide support was modified and optimized to produce the AuCNP ink, which is a dispersion of AuCNP and TNP in the mixture of EG and water. Despite the ink stability, it was revealed, that the ink age factor was critical for the AuNPs size distribution in the TiO_2 matrix. In order to obtain the AuNP imbedded in TiO_2/AuNP film with a mean size of 30 nm and minimal standard deviation, it was necessary to store the ink for at least 10 days after the synthesis. The TiO_2/AuNP films demonstrated a LSPR absorption in the yellow-green wavelength range. The proposed strategy opens up new possibilities for modifying the architecture of perovskite solar cells by introducing LSPR structures. That is a promising approach to increase the efficiency of photovoltaic devices.

Supplementary Materials: The following are available online at <https://www.mdpi.com/article/10.3390/coatings11121525/s1>, Figure S1: The images of the samples N1, N2, N3, and N5, Figure S2: Particle size distribution of colloidal TNP obtained by DLS, Figure S3: The image of the TiO₂/AuNP film ink-jet printed with 10-day-aged AuCNP ink on a glass substrate, Figure S4: The SEM images of the cross-section of the TiO₂/AuNP film, Figure S5: The day-age dependence of the AuCNP nanoparticles' HDD. The bars on the plot correspond to standard deviation. Reference [44] is cited in the supplementary materials.

Author Contributions: Methodology, S.R., A.M. and V.D.; experiment, S.R.; data analysis, S.R., V.D., A.M. and A.K.; supervision of the project, M.Z. All authors discussed the results and contributed to the final manuscript. All authors have read and agreed to the published version of the manuscript.

Funding: This research received no external funding.

Institutional Review Board Statement: Not applicable.

Informed Consent Statement: Not applicable.

Data Availability Statement: Data sharing is not applicable to this article.

Acknowledgments: The authors are deeply grateful to Yelena Yadgarov for helpful advice and fruitful discussions of the results, Natali Litvak for the SEM images, Alexey Kossenko for the XRD studies, and Michal Weitman (Bar Ilan University) for the TGA measurements. The research work of the student was carried out with the scholarship support of Yuri Dombrovsky.

Conflicts of Interest: The authors declare no conflict of interest.

References

1. Suchomel, P.; Kvitek, L.; Prucek, R.; Panacek, A.; Halder, A.; Vajda, S.; Zboril, R. Simple size-controlled synthesis of Au nanoparticles and their size-dependent catalytic activity. *Sci. Rep.* **2018**, *8*, 4589. [[CrossRef](#)] [[PubMed](#)]
2. Hu, X.; Zhang, Y.; Ding, T.; Liu, J.; Zhao, H. Multifunctional Gold Nanoparticles: A Novel Nanomaterial for Various Medical Applications and Biological Activities. *Front. Bioeng. Biotechnol.* **2020**, *8*, 990. [[CrossRef](#)] [[PubMed](#)]
3. Guo, Y.; He, X.; Liu, X.; Li, X.; Kang, L. One-step implementation of plasmon enhancement and solvent annealing effects for air-processed high-efficiency perovskite solar cells. *J. Mater. Chem. A* **2018**, *6*, 24036. [[CrossRef](#)]
4. Li, C.; Xu, C.; Cahen, D.; Jin, Y. Unprecedented efficient electron transport across Au nanoparticles with up to 25-nm insulating SiO₂-shells. *Sci. Rep.* **2019**, *9*, 18336. [[CrossRef](#)]
5. Yao, K. Plasmonic Metal Nanoparticles with Core-Bishell Structure for High-Performance Organic and Perovskite Solar Cells. *ACS Nano* **2019**, *13*, 5397–5409. [[CrossRef](#)] [[PubMed](#)]
6. Zhang, C.; Luo, Q.; Shi, J.; Yue, L.; Wang, Z.; Chena, X.; Huang, S. Efficient perovskite solar cells by combination use of Au nanoparticles and insulating metal oxide. *Nanoscale* **2017**, *9*, 2852–2864. [[CrossRef](#)]
7. Tran, Q.N.; Lee, H.K.; Kim, J.H.; Park, S.J. Influence of Gold-Silver Rough-Surface Nanoparticles on Plasmonic Light Scattering in Organic Solar Cells. *J. Nanosci. Nanotechnol.* **2020**, *20*, 304–311. [[CrossRef](#)]
8. Brown, M.D.; Suteewong, T.; Kumar, R.S.S.; D'Innocenzo, V.; Petrozza, A.; Lee, M.M.; Wiesner, U.; Snaith, H.J. Plasmonic Dye-Sensitized Solar Cells Using Core-Shell Metal-Insulator Nanoparticles. *Nano Lett.* **2011**, *11*, 438–445. [[CrossRef](#)]
9. Moakhar, R.S. Recent Advances in Plasmonic Perovskite Solar Cells. *Adv. Sci.* **2020**, *7*. [[CrossRef](#)]
10. Wang, B. Enhancing the Photovoltaic Performance of Perovskite Solar Cells Using Plasmonic Au@Pt@Au Core-Shell Nanoparticles. *Nanomaterials* **2019**, *9*, 1263. [[CrossRef](#)]
11. Sreedharan, R.S.; Kavitha, V.S.; Suresh, S.; Krishnan, R.R.; Bose, R.J.; Pillai, V.P.M. Tailoring the properties of zinc oxide films by incorporating gold nanoparticles using RF magnetron sputtering. *Appl. Phys. A* **2018**, *124*, 815. [[CrossRef](#)]
12. Li, J.; Zhou, H.; Qian, S.; Liu, Z.; Feng, J.; Jin, P.; Liu, X. Plasmonic gold nanoparticles modified titania nanotubes for antibacterial application. *Appl. Phys. Lett.* **2014**, *104*, 261110. [[CrossRef](#)]
13. Tan, B.J.Y.; Sow, C.H.; Koh, T.S.; Chin, K.C.; Wee, A.T.S.; Ong, C.K. Fabrication of Size-Tunable Gold Nanoparticles Array with Nanosphere Lithography, Reactive Ion Etching, and Thermal Annealing. *J. Phys. Chem. B* **2005**, *109*, 11100–11109. [[CrossRef](#)]
14. Bi, K. Direct electron-beam patterning of transferrable plasmonic gold nanoparticles using a HAuCl₄/PVP composite resist. *Nanoscale* **2019**, *11*, 1245. [[CrossRef](#)]
15. Keller, K.; Khramenkova, E.V.; Slabov, V.; Musin, A.; Kalashnikov, A.; Vinogradov, A.V.; Pidko, E.A. Inkjet Printing of Sc-Doped TiO₂ with Enhanced Photoactivity. *Coatings* **2019**, *9*, 78. [[CrossRef](#)]
16. Turkevich, J.; Stevenson, P.C.; Hiller, J. A study of the nucleation and growth processes in the synthesis of colloidal gold. *Discuss. Faraday Soc.* **1951**, *11*, 55–75. [[CrossRef](#)]
17. Kimling, J.; Maier, M.; Okenve, B.; Kotaidis, V.; Ballot, H.; Plech, A. Turkevich Method for Gold Nanoparticle Synthesis Revisited. *J. Phys. Chem. B* **2006**, *110*, 15700–15707. [[CrossRef](#)]

18. Brust, M.; Walker, M.; Bethell, D.; Schiffrin, D.J.; Whyman, R. Synthesis of Thiol-derivatised Gold Nanoparticles in a Two-phase Liquid-Liquid System. *J. Chem. Soc. Chem. Commun.* **1994**, *1994*, 801–802. [[CrossRef](#)]
19. Deraedt, C.; Salmon, L.; Gatard, S.; Ciganda, R.; Hernandez, R.; Ruiza, J.; Astruc, D. Sodium borohydride stabilizes very active gold nanoparticle catalysts. *Chem. Commun.* **2014**, *50*, 14194–14196. [[CrossRef](#)]
20. Fiévet, F. The polyol process: A unique method for easy access to metal nanoparticles with tailored sizes, shapes and compositions. *Chem. Soc. Rev.* **2018**, *47*, 5187–5233. [[CrossRef](#)]
21. Silvert, P.Y.; Tekcia-Elhissen, K. Synthesis of monodisperse submicronic gold particles by the polyol process. *Solid State Ionics* **1995**, *82*, 53–60. [[CrossRef](#)]
22. Sankar, M. Role of the Support in Gold-Containing Nanoparticles as Heterogeneous Catalysts. *Chem. Rev.* **2020**, *120*, 3890–3938. [[CrossRef](#)] [[PubMed](#)]
23. Buonerba, A.; Grassi, A. Trends in Sustainable Synthesis of Organics by Gold Nanoparticles Embedded in Polymer Matrices. *Catalysts* **2021**, *11*, 714. [[CrossRef](#)]
24. Haruta, M.; Tsubota, S.; Kobayashi, T.; Kageyama, H.; Genet, M.J.; Delmon, B. Low-Temperature Oxidation of CO Over Gold Supported on TiO₂, α -Fe₂O₃, and Co₃O₄. *J. Catal.* **1993**, *144*, 175–192. [[CrossRef](#)]
25. Soejima, T.; Tada, H.; Kawahara, T.; Ito, S. Formation of Au Nanoclusters on TiO₂ Surfaces by a Two-Step Method Consisting of Au(III)-Complex Chemisorption and Its Photoreduction. *Langmuir* **2002**, *18*, 4191–4194. [[CrossRef](#)]
26. Aguirre, M.E.; Perelstein, G.; Feldhoff, A.; Condó, A.; Tolley, A.J.; Grela, M.A. The spontaneous room temperature reduction of HAuCl₄ in ethylene glycol in the presence of ZnO: A simple strategy to obtain stable Au/ZnO nanostructures exhibiting strong surface plasmon resonance and efficient electron storage properties. *New J. Chem.* **2015**, *39*, 909. [[CrossRef](#)]
27. Pereira, J.M.d.S.; Ciotti, L.; Vaz, J.M.; Spinacé, E.V. Preparation of Au/TiO₂ Catalyst by a Liquid-Phase Reduction Method for Preferential Oxidation of Carbon Monoxide in a Hydrogen Rich-Stream (CO-PROX reaction). *Mater. Res.* **2018**, *21*. [[CrossRef](#)]
28. Haruta, M. Size- and support-dependency in the catalysts of gold. *Catal. Today* **1997**, *36*, 153–166. [[CrossRef](#)]
29. Haruta, M. Role of perimeter interfaces in catalysis by gold nanoparticles. *Faraday Discuss.* **2011**, *152*, 11–32. [[CrossRef](#)]
30. Brar, K.S.; Verma, M. Measurement of nanoparticles by light-scattering techniques. *Trends Anal. Chem.* **2011**, *30*, 4–17. [[CrossRef](#)]
31. Xu, R. Progress in nanoparticles characterization: Sizing and zeta potential measurement. *Particuology* **2008**, *6*, 112–115. [[CrossRef](#)]
32. Murphy, P.J.; LaGrange, M.S. Raman spectroscopy of gold chloro-hydroxy speciation in fluids at ambient temperature and pressure: A re-evaluation of the effects of pH and chloride concentration. *Geochim. Cosmochim. Acta* **1998**, *62*, 3515–3526. [[CrossRef](#)]
33. Ivanova, S.; Petit, C.; Pitchon, V. A new preparation method for the formation of gold nanoparticles on an oxide support. *Appl. Catal. A Gen.* **2004**, *267*, 191–201. [[CrossRef](#)]
34. Zanella, R.; Giorgio, S.; Henry, C.R.; Louis, C. Alternative Methods for the Preparation of Gold Nanoparticles Supported on TiO₂. *J. Phys. Chem. B* **2002**, *106*, 7634–7642. [[CrossRef](#)]
35. Mazza, T.; Barborini, E.; Piseri, P.; Milani, P.; Cattaneo, D.; Li Bassi, A.; Ducati, C. Raman spectroscopy characterization of TiO₂ rutile nanocrystals. *Phys. Rev. B* **2007**, *75*, 045416. [[CrossRef](#)]
36. Krishnan, K.; Krishnan, R.S. Raman and infrared spectra of ethylene glycol. *Proc. Indian Acad. Sci. Sect. A* **1966**, *64*, 111–123. [[CrossRef](#)]
37. Hoath, S.D. Fundamentals of Inkjet Printing. In *The Science of Inkjet and Droplets*; Wiley: Weinheim, Germany, 2016; p. 98. [[CrossRef](#)]
38. Reis, N.; Derby, B. Ink jet deposition of ceramic suspensions: Modelling and experiments of droplet formation. *Mater. Res. Soc. Symp. Proc.* **2000**, *625*, 117–122. [[CrossRef](#)]
39. Jang, D.; Kim, D.; Moon, J. Influence of fluid properties on ink-jet printability. *Langmuir* **2009**, *25*, 2629–2635. [[CrossRef](#)] [[PubMed](#)]
40. Kim, D.-K.; Hwang, Y.J.; Yoon, C.; Yoon, H.-O.; Chang, K.S.; Lee, G.; Lee, S.; Yi, G.-R. Experimental approach to the fundamental limit of the extinction coefficients of ultra-smooth and highly spherical gold nanoparticles. *Phys. Chem. Chem. Phys.* **2015**, *17*, 20786–20794. [[CrossRef](#)]
41. Lavie, A.; Yadgarov, L.; Houben, L.; Popovitz-Biro, R.; Shaul, T.E.; Nagler, A.; Suchowski, H.; Tenne, R. Synthesis of core-shell single-layer MoS₂ sheathing gold nanoparticles, AuNP@ 1L-MoS₂. *Nanotechnology* **2017**, *28*, 24LT03. [[CrossRef](#)]
42. Aiboushev, A.; Gostev, F.; Shelaev, I.; Kostrov, A.; Kanaev, A.; Museur, L.; Traore, M.; Sarkisova, O.; Nadtochenko, V. Spectral properties of the surface plasmon resonance and electron injection from gold nanoparticles to TiO₂ mesoporous film: Femtosecond study. *Photochem. Photobiol. Sci.* **2012**, *12*, 631–637. [[CrossRef](#)] [[PubMed](#)]
43. Bonkerud, J.; Zimmermann, C.; Weiser, P.M.; Vines, L.; Monakhov, E.V. On the permittivity of titanium dioxide. *Sci. Rep.* **2021**, *11*, 12443. [[CrossRef](#)] [[PubMed](#)]
44. Behnajady, M.A.; Eskandarloo, H.; Modirshahla, N.; Shokri, M. Sol-gel low-temperature synthesis of stable anatase-type TiO₂ nanoparticles under different conditions and its photocatalytic activity. *Photochem. Photobiol.* **2011**, *87*, 1002–1008. [[CrossRef](#)] [[PubMed](#)]